BEAM POINTING INSTABILITY OF HIGH-POWER END-PUMPED 1064 nm ND : YAG LASER

Zheyuan Li, Peijin Shang, Shiyu Wang,* **He Qiao, Bing bin Li, Qian Guo, Defang Cai, Lequn Li, and Fuqiang Ma**

School of Optoelectronic Engineering, XiDian University
Xi'an Shaanxi 710071, China

*Corresponding author e-mail: xadzlzy @ 163.com

Abstract

In this paper, we propose a numerical calculation model, which considers thermal and gain distribution instabilities and inhomogeneities, for analyzing beam pointing instability in Nd : YAG solid-state lasers. Disturbance factors are defined for pumping power and pumping field, representing their degrees of disturbance. We discuss a numerical example to calculate the beam pointing instability for a positive branch confocal unstable resonator. Subsequently, an optimization design method is discussed for minimizing beam pointing fluctuation in a resonant cavity. This method incorporates considerations of thermal and gain distribution instabilities and inhomogeneities, thus offering a straightforward design approach with broad applicability.

Keywords: beam pointing stability, high-power Nd : YAG lasers, thermal instability, gain instability.

1. Introduction

Recently, high-power solid-state lasers have garnered significant attention owing to their vital roles in military and scientific research [1–5]. Among these lasers, high-power solid-state Nd : YAG lasers have emerged as key assets for military operations and find widespread applications in fields, such as laser material processing, measurements, cutting, spectroscopy analysis, optical communication, and others [6–12]. These lasers are valued for their compact design, longevity, efficient energy conversion, stable output, resilience to external conditions, superior beam quality, and broad crystal coverage.

For high-power solid-state lasers, particularly those suited for long-distance battlefield environments, in addition to high power and high beam quality, the high beam pointing stability is of paramount importance, as it directly impacts the efficacy of laser weapons. However, existing research on this aspect remains limited. In 2016, Ding et al. utilized a scientific-grade charge-coupled device (CCD) to investigate the beam pointing stability within a single-shot nanosecond-level high-power Nd : glass laser system; the output beam diameter was 60 mm with 100 J laser energy at 1053 nm. The study reported A root mean square (RMS) value of the long-term angle drift in the output laser beam to be smaller than 17 µrad. Nonetheless, a comprehensive exploration of factors influencing beam pointing instability was lacking [13]. In 2019, Xie et al. delved into the application of high-precision laser-beam pointing technology in the airborne aiming pods. Their findings revealed a maximum pointing error of 0.015° and RMS value of 0.0075°. Their investigation primarily investigated the impact of aircraft disturbances and atmospheric turbulence on beam directionality, without delving into the effects of laser disturbances on output beam direction [14]. A seminal study by Dixit et al. in 2008 provided a comprehensive analysis

---

of pointing stability in Copper vapor lasers, with a focus on the role of the optical resonator. Results indicated that a minimum beam pointing angle of 8 μrad was obtained with the generalized diffraction filtered resonator (GDFR), in contrast to a maximum value of 120 μrad from the plane–plane resonator; unstable resonators yielded intermediate values. However, the study also omitted consideration of the instabilities and inhomogeneities in thermal and gain distributions and their impact on beam pointing instability [15].

In this study, we introduce a numerical calculation model aimed at analyzing beam pointing instability, while considering the instabilities and inhomogeneities in the distribution of temperature and gain. The gain within the gain medium is intricately linked to the population inversion density, which is determined by the pump energy's absorption. A part of leftover energy transforms into waste heat, thus resulting in an uneven temperature field within the crystal. Ideally, temperature and gain distributions maintain axis-symmetric patterns, essentially ensuring that the laser beam aligns perfectly with the optical axis. However, in practical situations involving end-pumped lasers, disturbance in pumping power and pumping field induces unstable and non-uniform temperature and gain distributions. This results in laser-beam pointing deviations. To quantify these disturbances, we define the pumping power disturbance factor and the pumping field disturbance factor, thereby signifying the extent of disruption in each parameter. For water-cooled lasers, the Nd:YAG crystal is placed in a copper radiator, which absorbs and temporarily stores the heat from the crystal through a flow of cold water. Employing the finite difference method [16, 17] and rate equation [18], we calculated the transient temperature field and gain distribution within the gain medium during the pumping phase. The classical numerical method of the Fox–Li open-cavity mode algorithm [19–22] is effective for calculating the laser mode. We perform this calculation by considering thermal and gain instability, as well as inhomogeneity, and solving the motion equation of laser oscillation in the cavity. The positive branch confocal unstable cavity – a typical high-power laser cavity configuration – is chosen as an illustrative example for studying beam pointing instability.

Subsequently, combined with the cubic spline interpolation method, we propose an optimization design approach for resonant cavity parameters that minimizes beam pointing fluctuations. This method considers the instabilities and inhomogeneities in temperature and gain distributions. We provide an algorithm flowchart and present a simulation example to demonstrate the practical application of our approach.

2. Establishment of Positive Branch Confocal Unstable Resonator Model

The resonant cavity is a crucial aspect in the design of high-power solid-state lasers. Although a stable cavity is typically employed at medium to low pumping power levels, its usage at high pumping power levels can lead to significant degradation of laser beam quality. The incorporation of a mode-limiting element to improve beam quality within the stable cavity leads to a reduced mode volume and efficient energy conversion. In contrast, an unstable resonator offers a solution by concurrently achieving superior beam quality and heightened energy conversion efficiency, thereby addressing the design complexities of high-power solid-state lasers [23].

Among the resonator cavity types suitable for high-power solid-state laser engineering, the positive branch confocal unstable resonator is a crucial one [24,25]. Under ideal conditions, this resonator produces a parallel output beam according to the unstable cavity's conjugate image point theory, essentially yielding

a divergence angle of zero. This facilitates attainment of higher beam quality, whereas the absence of a focal point within the unstable resonator cavity prevents, optical element damage is not easily caused by erroneous operation. Consequently, equipment reliability is enhanced.
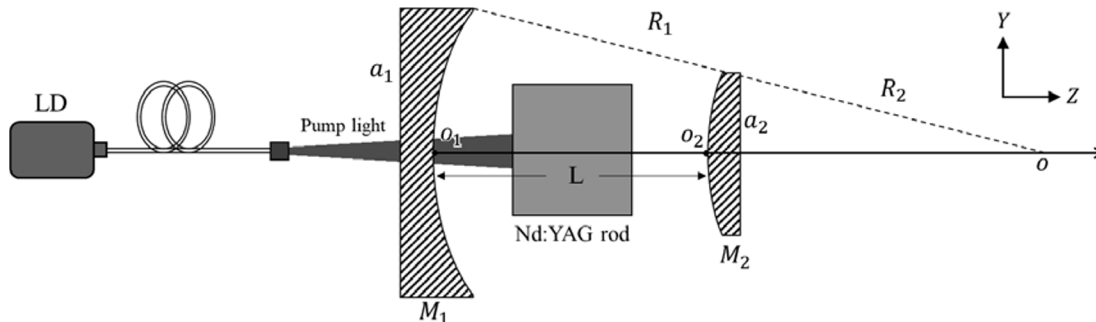

Fig. 1. Positive branch confocal unstable resonator.

As shown in Fig. 1, the positive branch confocal unstable resonator takes the form of a typical concave-convex cavity configuration. Here, M_1 represents a reflector mirror possessing the radius of curvature R_1, whereas M_2 corresponds to an output coupler with the radius of curvature R_2 $(R_2 < 0)$. These mirrors are both designed as all-reflective mirrors, featuring 100% reflectivity to facilitate oscillating light. Notably, the beam emerges epitaxially from the output coupler. The two mirrors exhibit an external confocal arrangement with the common focal point O. Leveraging this confocal characteristic, the cavity length L assumes a value of $(R_1 + R_2)/2$, and the equivalent Fresnel number N_{eq} can be expressed as $(a_1 + a_2)/\lambda L$, where a_1 and a_2 denote the half-widths of the square reflector mirror and the square output coupler, respectively, essentially satisfying the condition $a_1 = a_2 \cdot R_1/(-R_2)$.

The beam pointing of the laser is defined as the straight line between the center of the output coupler and the gravity center of the far-field spot. The coordinates of the gravity center of the far-field spot are as follows:

$$\hat{x} = \frac{\displaystyle\int xI(x,y)\,dx\,dy}{\displaystyle\int I(x,y)\,dx\,dy}, \qquad \hat{y} = \frac{\displaystyle\int yI(x,y)\,dx\,dy}{\displaystyle\int I(x,y)\,dx\,dy}. \tag{1}$$

In paraxial conditions, the tangent of a small angle (measured in Radians) is approximately equal to the angle, that is, $\tan\theta \approx \theta$. The beam pointing drift angle is defined as

$$\theta = \frac{\sqrt{\hat{x}^2 + \hat{y}^2}}{z}. \tag{2}$$

3. Theoretical Analysis of the Disturbance Factor and Instability

As shown in Fig. 2, the crystal is approximated as an aperture diaphragm, with thickness considerations set aside. As the oscillating beam traverses this diaphragm, it undergoes modulation stemming from both the gain and thermal fields. This modulation can be expressed as follows:

$$U'(x,y) = W(x,y)F(x,y)U(x,y), \tag{3}$$

where $U(x, y)$ is the oscillating optical field entering the aperture diaphragm, $U'(x, y)$ is the oscillating optical field exiting in the aperture diaphragm, and $W(x, y)$ and $F(x, y)$ denote the modulation functions corresponding to the gain and thermal fields, respectively. These functions can be defined in the subsequent manner,

$$W(x, y) = \exp(G(x, y)), \qquad F(x, y) = \exp(-i\Delta\phi(x, y)), \tag{4}$$

where $G(x, y)$ is the single-pass gain, and $\Delta\phi(x, y)$ is the single-pass additional phase difference arising from the thermal effects within the crystal.
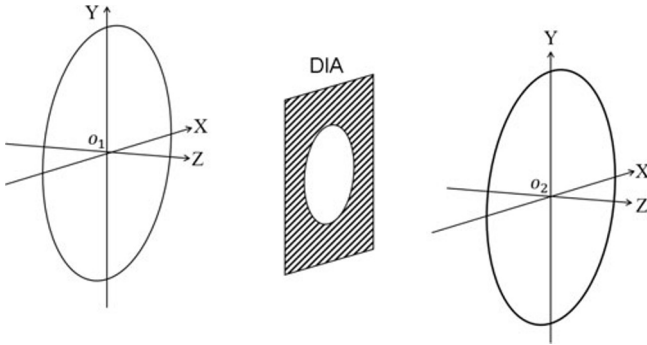

Fig. 2. Crystal and cavity model.

In the case of LD end-pumped Nd:YAG lasers, the entirety of the pumping energy absorbed by the gain medium does not transform into laser output owing to phenomena such as the quantum defect effect and fluorescence quenching effect. Instead, a significant proportion is deposited within the gain medium as waste heat. This heat distribution follows a density function [26, 27]; it reads

$$q(x, y, z) = P_{in}\eta(1 - \exp(-\alpha l))I(x, y, z), \tag{5}$$

where P_{in} is the pumping power directed into the Nd:YAG rod, η is the thermal conversion coefficient, α is the absorption coefficient for the pump light, l is the length of the Nd:YAG rod, and $I(x, y, z)$ is the pumping intensity. This normalized function can be expressed as

$$I(x, y, z) = \frac{2\alpha}{\pi\omega_p^2 \left[1 - \exp(-\alpha l)\right]} \cdot \left[\exp\left(-2\left(\frac{x^2 + y^2}{\omega_p^2}\right)\right)\right] \exp(-\alpha z), \tag{6}$$

where ω_p is the radius of the pump light. Considering the absorption of pump light along the axial direction and heat dissipation from the side face of the Nd:YAG rod, we can omit the heat flow along the axial direction; this results in a simplified form of the heat conduction equation [28],

$$\gamma \cdot \left(\frac{\partial^2 T(x, y)}{\partial x^2} + \frac{\partial^2 T(x, y)}{\partial y^2}\right) + q(x, y) = \rho C \frac{\partial T(x, y)}{\partial t}, \tag{7}$$

where $T(x, y)$ represents the internal temperature of the Nd:YAG rod, γ represents the thermal conductivity, ρ represents the crystal density, and C represents the heat capacity of the crystal. The finite difference method [16, 17] proves to be an effective approach for solving the heat conduction equation. As shown in Fig. 3, the crystal's end face is partitioned into $(n - 1) \times (m - 1)$ mesh regions. Nodes are established at the intersections of grid lines, with the step size h. The coordinates of these nodes are given by $(x, y) = (ih, jh)$, where $i = 0, 1, \ldots, n$ and $j = 0, 1, \ldots, m$, which can be expressed as (i, j).

The temperature at node (i, j) is $T_{i,j}$. Following the principles of the finite difference method, the second-order partial derivative of $T_{i,j}$ can be estimated through the difference between $T_{i+1,j}$, $T_{i-1,j}$, $T_{i,j+1}$, $T_{i,j-1}$, and $T_{i,j}$, in view of the following expression:

$$\frac{\partial^2 T_{i,j}}{\partial x^2} + \frac{\partial^2 T_{i,j}}{\partial y^2} \approx \frac{T_{i+1,j} + T_{i-1,j} + T_{i,j+1} + T_{i,j-1} - 4T_{i,j}}{h^2}. \tag{8}$$
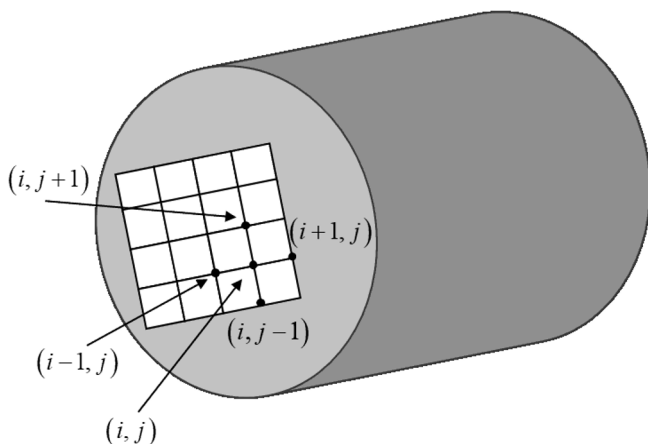
Fig. 3. Finite difference grid.

The pump time t is divided into u steps with the step size h_t, namely,

$$t = ph_t; \qquad p = 0, 1 \ldots u. \tag{9}$$

The temperature at time t is $T_{i,j,p}$, and its time derivative is approximated by the difference quotient, which can be expressed as follows:

$$\frac{\partial T_{i,j,p}}{\partial t} = \frac{T_{i,j,p+1} - T_{i,j,p}}{h_t}. \tag{10}$$

By incorporating Eqs. (8) and (10) into Eq. (7), the iterative equation governing heat conduction can be represented as

$$T_{i,j,p+1} = T_{i,j,p} + \frac{h_t\gamma}{\rho C h^2}\left(T_{i+1,j,p} + T_{i-1,j,p} + T_{i,j+1,p} + T_{i,j-1,p} - 4T_{i,j,p}\right) + \frac{h_t}{\rho C}q_{i,j,p}, \tag{11}$$

where $q_{i,j,p}$ is the heat source intensity of node (i, j) at time t. Within the Nd:YAG rod, alterations in the temperature field prompt shifts in the crystal's refractive index, which causes the change of the optical path difference (OPD), when the oscillating beam traverses the gain medium, and ultimately introduces the additional phase difference to the oscillating beam within the cavity. The expression for the single-pass additional phase difference reads

$$\Delta\phi(x,y) = \frac{2\pi}{\lambda}\mathrm{OPD} = \frac{2\pi}{\lambda}\int_0^l \Delta n(x,y,z)\, dz \ \ \Delta n(x,y,z) = \frac{dn}{dT}\left[T(x,y,z) - T(0,0,z)\right], \tag{12}$$

where $T(0,0,z)$ is the temperature along the central axis of the crystal, λ is the wavelength, and $\dfrac{dn}{dT}$ is the temperature dependent of the refractive index.

According to the rate equation [18], the single-pass gain of the laser oscillation can be expressed as follows:

$$G(x,y) = \sigma\int_0^l N_0(x,y,z)dz = \frac{\sigma\tau}{E_0}P_{in}[1 - \exp(-\alpha l)]\left[1 - \exp\left(-\frac{t}{\tau}\right)\right]\int_0^l \frac{\partial I(x,y,z)}{\partial z}\, dz, \tag{13}$$

where σ is the stimulated absorption cross section, $N_0(x,y,z)$ is the population inversion density, τ is the lifetime of the upper-level population, and E_0 is the single photon energy of the pump light.

We employ the well-established classical Fox–Li open-cavity mode iterative algorithm, centered around the Fresnel–Kirchhoff diffraction formula, to compute the distribution of the output optical field. This approach yields results closely aligned with engineering experiments, showcasing only minor deviations. As shown in Fig. 4, the algorithm's formulation is presented as [19, 20]

$$U_{\mathrm{DIA}}(x,y) = \frac{\mathrm{i}k}{4\pi}\iint_{S_1} U_1(x',y')\frac{e^{-ik\mu}}{\mu}(1 + \cos\beta)\, ds, \tag{14}$$

where S_1 is the area of the reflector mirror M_1, $U_1(x', y')$ is the optical field distribution at M_1, $U_{\text{DIA}}(x, y)$ is the optical field distribution at the aperture diaphragm before modulation, k is the wave number of the oscillating beam; μ is the distance between the points (x', y') and (x, y), and β is the angle between the normal $\vec{n}$ and $\vec{\mu}$ at the point (x', y'). When considering the curvature radius of the reflector mirror, the expressions for μ and $\cos \beta s$ in Eq. (14) become

$$\mu = \sqrt{(x' - x)^2 + (y' - y)^2 + (z' - z)^2},$$
$$\cos \beta = \frac{(-x')(x - x') + (-y')(y - y') + (R_1 - z')(z - z')}{R_1 \sqrt{(x - x') + (y - y') + (z - z')}}, \tag{15}$$

and the laser oscillates in the resonant cavity to achieve stimulated amplification. If the oscillation achieves a steady state, the light field motion equation in the resonant cavity can be expressed as follows:

$$\delta_a U_1 = \left(\frac{\mathrm{i}k}{4\pi}\right)^4 \iint\limits_{S_{\text{DIA}}} \exp(G) \exp(-i\Delta\phi) \frac{e^{-ik\mu_{D1}}}{\mu_{D1}} (1 + \cos\beta_{D1}) \, ds_{\text{DIA}} \times \iint\limits_{S_2} \frac{e^{-ik\mu_{2D}}}{\mu_{2D}} (1 + \cos\beta_{2D}) \, ds_2$$

$$\times \iint\limits_{S_{\text{DIA}}} \exp(G) \exp(-i\Delta\phi) \frac{e^{-ik\mu_{d2}}}{\mu_{d2}} (1 + \cos\beta_{D2}) \, ds_{\text{DIA}} \times \iint\limits_{S_1} \frac{e^{-ik\mu_{1D}}}{\mu_{1D}} (1 + \cos\beta_{1D}) U_1 \, ds_1, \tag{16}$$

where μ_{ij}; $i, j = 1, 2, D$ and β_{ij}; $i, j = 1, 2, D$ are the distance and angle between the reflector mirror, output coupler, and equivalent aperture, respectively, and δ_a; $a = 1, 2, 3, 4, \ldots$ are eigenvalues. The basic-mode Gaussian function of the light field obtained from this equation is the fundamental mode of the laser.
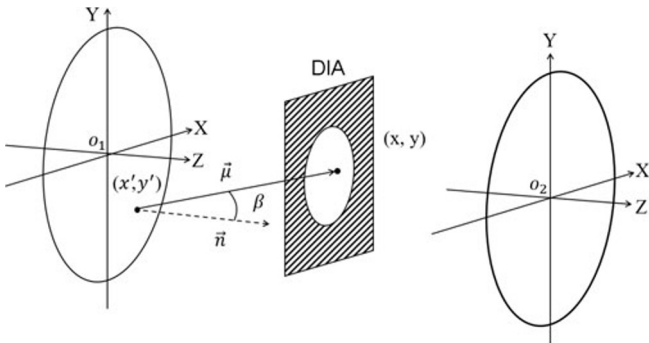

Fig. 4. Positive branch confocal unstable resonator Fox–Li algorithm model.

In the case of quasi-continuous operating lasers, various factors inevitably disrupt the pumping power and pumping field. Examples include fluctuations in pump current and poor heat dissipation of pump. The disturbance of pumping power and pumping field can be expressed as

$$P_{\text{real}}(t) = P_{\text{in}}\varepsilon_1(t),$$
$$I_{\text{real}}(x, y, z, t) = I(x, y, z)\varepsilon_2(x, y, z, t), \tag{17}$$

where $\delta_a(a = 1, 2, 3, 4, \ldots)$ and $\varepsilon_2(x, y, z, t)$ are designated as the pumping power disturbance coefficient and the pumping field disturbance coefficient, respectively. These coefficients can be defined as

$$\varepsilon_1(t) \sim U(1 - \xi_1, 1 + \xi_1), \qquad \varepsilon_2(x, y, z, t) \sim U(1 - \xi_2, 1 + \xi_2), \qquad 0 \le t \le t_0,$$
$$\varepsilon_1(t) = \varepsilon_2(x, y, z, t) = 1, \qquad t > t_0, \tag{18}$$

where ξ_1 is the pumping power disturbance factor, ξ_2 is the pumping field disturbance factor, and t_0 is the pumping duration.

4. Simulation Analysis of the Beam Pointing Instability

4.1. Ideal Pumping Conditions

We utilize MATLAB software to simulate the heat conduction process within the end-pumped water-cooled Nd:YAG rod. The absorption coefficient α of the Nd:YAG rod is set equal to 0.73 mm^{-1} and thermal conversion coefficient η equal to 0.32; the length l of the Nd:YAG rod is 10 mm; and pump light radius ω_p is 1.5 mm. Also, r is the radial length of the Nd:YAG rod. In Fig. 5, we show the heat source intensity calculated, using Eq. (5), for various pumping powers.
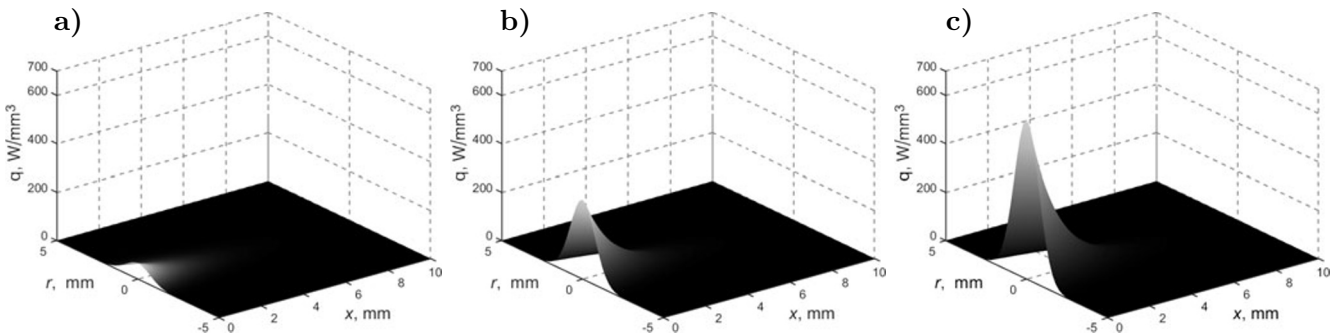

Fig. 5. Heat source intensity of the pump-end face with different pumping power. Here, $P_{\text{in}} = 1000$ W (a), 5000 W (b), and 10000 W (c).

Set the thermal conductivity of the Nd:YAG rod $\gamma = 0.013$ W/(mm$\cdot$K), the crystal density $\rho = 4.5 \cdot 10^{-3}$ g/mm^3, the specific heat capacity $C = 0.56$ J/(g$\cdot$K), the diameter of the Nd:YAG rod $d = 10$ mm, the spatial step $h = 0.2$ mm, the corresponding time step $h_t = 3 \cdot 10^{-8}$ s, and the grid quantity for simulation is 50×50.

The Nd:YAG crystal rods are placed in a copper heat sink. The heat source intensity in the region $r < d/2$ is $q_{i,j,p}$; whereas, it is zero in the region $r \geq d/2$, because this is in the heat sink portion. The initial temperature across all nodes, as well as that of the heat sink, is set to 300 K. For simplicity, we neglect the complexities introduced by nonuniform and intricate thermal contact resistance between the crystal and heat sink. This allowed us to employ Dirichlet boundary conditions for simulation, maintaining the boundary temperature of the cylindrical surface at 300 K.

Note that Eq. (11) is resolved during a pump duration of 200 µs. In Fig. 6, we illustrate the changes in temperature at the crystal's end face across different pumping powers. Notably, the temperature at the crystal's end face displays linear and symmetrical variation throughout the pumping duration. Thus, the most rapid temperature increase pumping occurs at the center of the crystal's end face.

We set the temperature dependence of refractive index $\dfrac{dn}{dT} = 7.3 \cdot 10^{-6}$ K^{-1}, the wavelength $\lambda = 1064$ mm, and pumping power $P_{\text{in}} = 10000$ W. Combined with the calculations of temperature field distribution in Fig. 6, the additional phase differences, computed using Eq. (12), exhibit analogous axis symmetric profiles across varying pump times. This behavior is shown in Fig. 7.

Set the stimulated absorption cross section $\sigma = 5.3 \cdot 10^{-18}$ mm^2, single photon energy $E_o = 2.46 \cdot 10^{-19}$ J, lifetime of upper-level population $\tau = 230$ µs, and pumping power $P_{\text{in}} = 10000$ W. In Fig. 8, we present the gain profiles corresponding to different pump times computed, using Eq. (13); here, these profiles also exhibit axis symmetric characteristics.
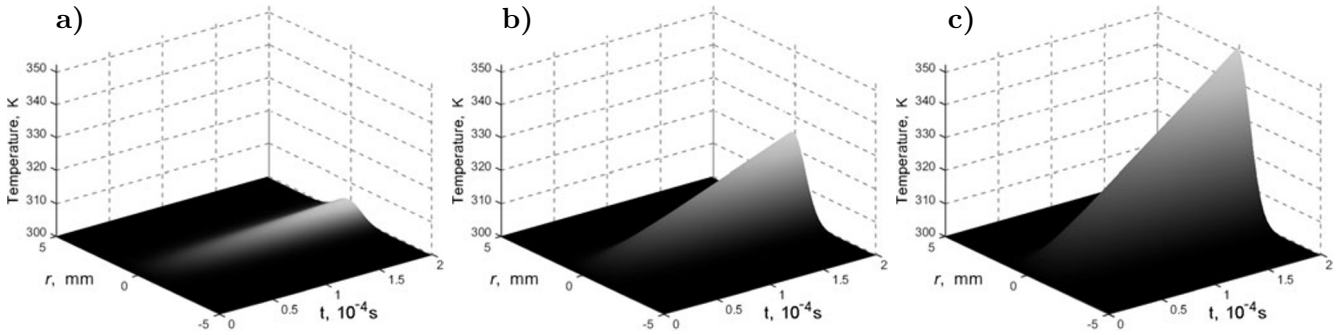
Fig. 6. Variation in temperature with different pumping powers $P_{\text{in}} = 1000$ W (a), 5000 W (b), and 10000 W (c).
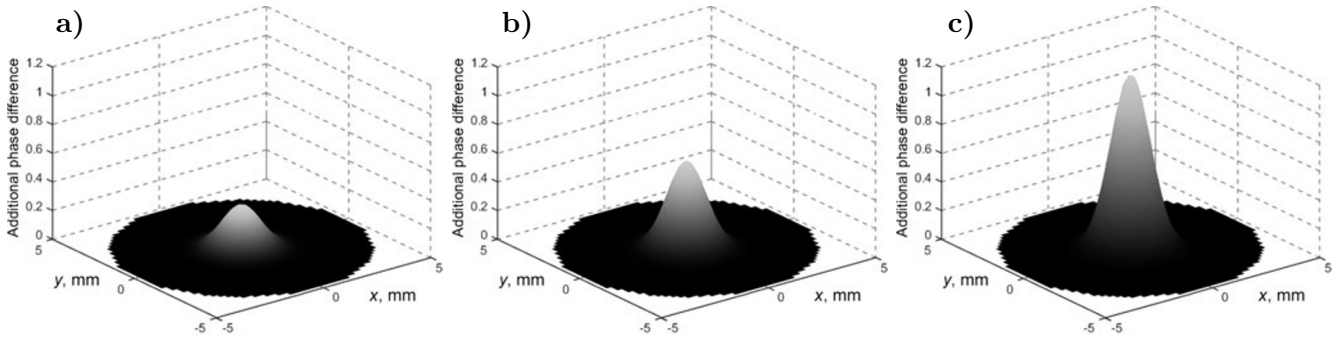

Fig. 7. Additional phase difference profiles at different pump times. Here, $t = 50$ μs (a), 100 μs (b), and 200 μs (c).

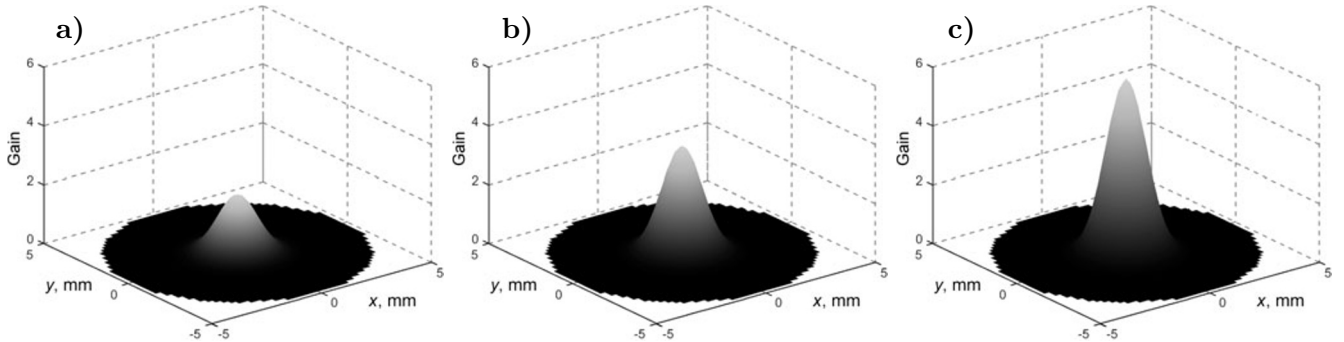**Fig. 8.** Gain profiles at different pump times. Here, $t = 50$ μs (a), 100 μs (b), and 200 μs (c).

Next, we consider the following parameter settings. The length of the positive branch confocal unstable resonator length is 200 mm, curvature radius of reflector mirror is 900 mm, and output coupler curvature radius is 500 mm; also equivalent Fresnel number $N_{\text{eq}} = 6.0903$, pump duration $t_0 = 200$ μs, and pumping power $P_{\text{in}} = 10000$ W. With these parameter settings, the calculation of the output optical field distribution and beam pointing drift angle are feasible according to Eq. (16). In the context of the positive branch confocal unstable cavity operating under ideal pumping conditions, the distributions of the temperature field and gain field demonstrate axis symmetric properties. Consequently, the output optical field consistently maintains an axis symmetric distribution, thus ensuring that the beam pointing drift angle remains at zero under these ideal pumping conditions.

4.2. Pump with Disturbances

To obtain the heat source and light field distributions under the condition of pump disturbance, we substitute Eq. (17) into Eqs. (5) and (6). Under the simulation conditions described in Sec. 4.1, we perform calculations, using Eq. (12). The profiles of the additional phase difference at the end of the pump cycle are displayed in Fig. 9, essentially illustrating variations under different pump disturbance factors. One can see that, under perturbation conditions, the axis symmetry of these profiles observed under ideal pumping conditions no longer holds; this conclusion applies to the gain profiles as well.
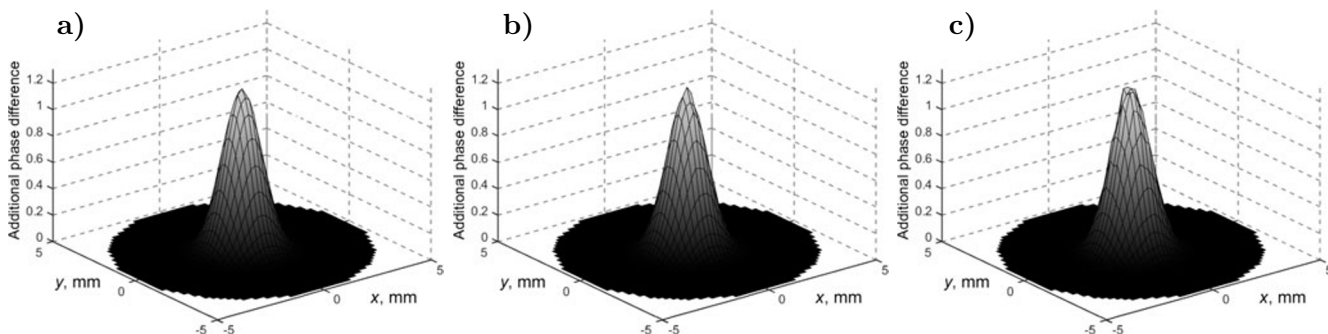

Fig. 9. Additional phase difference profiles with different disturbance factors at the end of the pump duration. Here, $\xi_1 = \xi_2 = 0.01$ (a), 0.03 (b), and 0.05 (c).

Set the disturbance factors $\xi_1 = \xi_2 = 0.01$, and the pump duration $t = 2 \cdot 10^{-4}$ s. Referring to the above calculation method, we substitute the nonuniform thermal effect and gain results at different times into Eq. (16) and calculate the laser mode under pump disturbance at different times, in view of Eq. (12). The plots illustrating the beam pointing drift angle as a function of time in a single pump duration, under varying pumping powers, are presented in Fig. 10 a. In another scenario, assuming the pumping power $P_{\mathrm{in}} = 10000$ W, the plots depicting beam pointing drift angle versus time in a single pump duration, considering different disturbance factors, are displayed in Fig. 10 b. Owing to the stochastic nature of pump power and pump field disturbances in a single pump duration, multiple repetitions of the simulation experiment must be conducted to derive the RMS value, which reflects the statistical attributes. After performing 100 times operation, the averaged statistical outcomes are showcased in Fig. 10. Notably, the drift angle of the pump light experiences pronounced fluctuations throughout the entire pump duration, with the fluctuation intensifying as the pump time increases, and the jitter becoming increasingly prominent. When disturbance factors are held constant, larger pumping powers yield greater jitter in the beam pointing drift angle. Similarly, with constant pumping power, higher disturbance factors lead to increased jitter in the beam pointing drift angle.

To delve deeper into the impact of pumping power P_{in}, pumping power disturbance factor ξ_1, and pumping field disturbance factor ξ_2 on the beam pointing drift angle, an in-depth analysis is undertaken. The beam-pointing drift angle fluctuation range is defined as the disparity between the maximum and minimum values of the beam-pointing drift angle θ [in Radians] within a single pump duration. If pump duration $t = 2 \cdot 10^{-4}$ s, the variation mesh surface detailing the range of beam-pointing drift angle fluctuations with respect to ξ_2 and P_{in} is visualized in Fig. 11, for a case where $\xi_2 = 0.01$. This fluctuation range serves as the assessment parameter for beam pointing stability. Evidently, a heightened value of P_{in} corresponds to an expanded beam pointing drift angle fluctuation range, indicative of diminished beam pointing stability. In contrast, the influence of ξ_1 on beam pointing stability is relatively modest; instead,
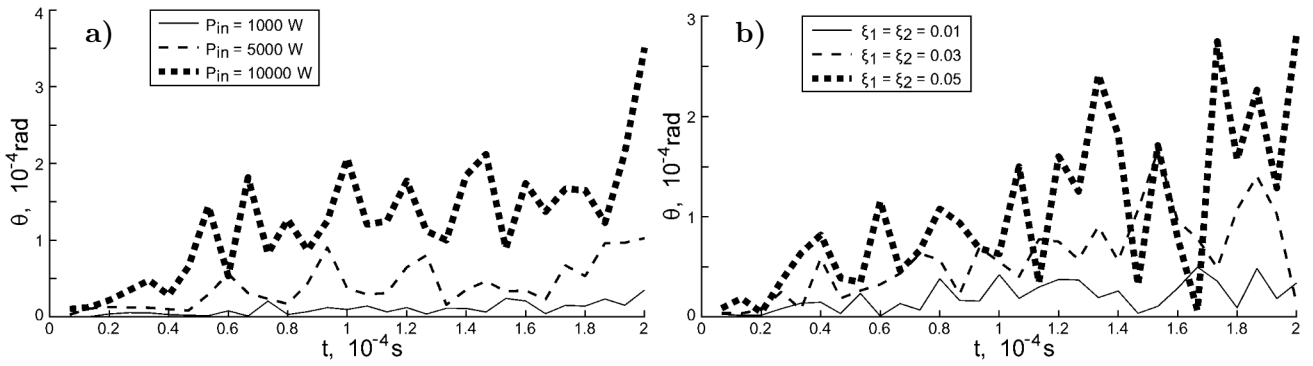
Fig. 10. Variation curves of beam pointing drift angle versus time with different pumping power at $\xi_1 = \xi_2 = 0.01$ (a) and different disturbance factors at $P_{\text{in}} = 10000$ W (b).
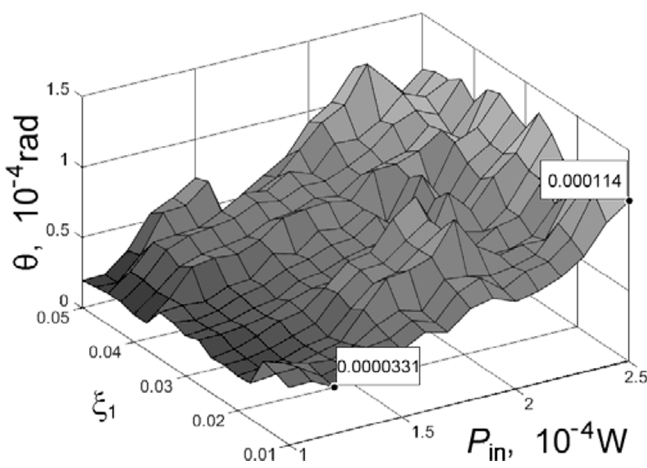
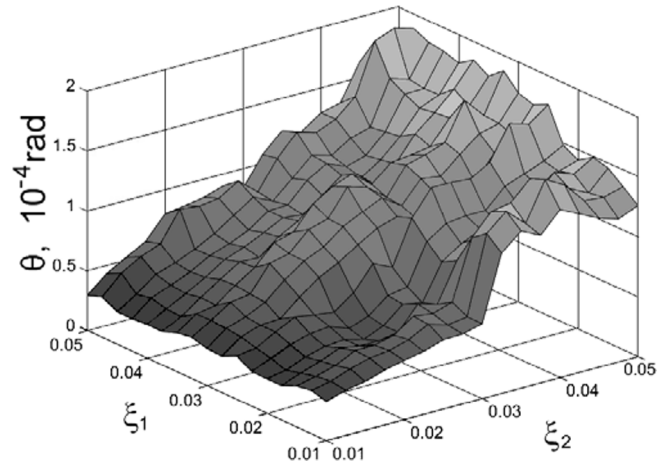**Fig. 11.** Beam pointing drift angle [in Radians] versus ξ_1 and P_{in}.

Fig. 12. Beam pointing drift angle [in Radians] versus ξ_1 and ξ_2.

it primarily shapes the extent of variation in beam pointing stability. Amplified ξ_1 values result in a more pronounced range of variation in beam pointing stability. For example, when $\xi_1 = 0.01$, 0.03, and 0.05, the variation range of the beam pointing stability is $8.09 \cdot 10^{-5}$ rad, $8.83 \cdot 10^{-5}$ rad, and $10.47 \cdot 10^{-5}$ rad, respectively.

Assuming that the pumping power $P_{\text{in}} = 10000$ W, we show in Fig. 12 the influence of ξ_1 and ξ_2 on the beam pointing stability. Evidently, an increased ξ_2 value corresponds to a deterioration in beam pointing stability. As observed in Fig. 11, ξ_1 has minimum influence on beam pointing stability; however, it significantly shapes the variation of beam pointing stability concerning ξ_2. Notably, heightened ξ_1 values lead to a broader range of variation in beam pointing stability. For example, when $\xi_1 = 0.01$, 0.03, and 0.05, the variation range is $10.7 \cdot 10^{-5}$ rad, $14.3 \cdot 10^{-5}$ rad, and $15.2 \cdot 10^{-5}$ rad, respectively.

The simulation outcomes confirm that the disturbance factors ξ_1 and ξ_2 defined in this study align with the underlying physical principles. These factors quantitatively capture the perturbations in pumping power and pump field, thus offering a means to quantify the impact of external disturbances on beam pointing stability. In the actual measurement, $P_i; i = 1, 2, \ldots, n$ is the pump source power of a single measurement, n is the number of measurements, and P_{in} is the average power of n measurements. Therefore, $\varepsilon_{1i} = p_i / p_{\text{in}}$. The uniform distribution $U(1 - \xi_1, 1 + \xi_1)$, which is equivalent to the mean and

standard deviation of n measurements related to P_i, is used to describe the disturbance of the actual power of the pump source. Similarly, the distribution of the pump source field is divided into two-dimensional grids. $I_j(x, y, z); j = 1, 2, \ldots, n$ is the pump source light intensity measured by a single node, n is the number of measurements, and $I_{\text{in}}(x, y, z)$ is the average light intensity of a single node. Therefore, $\varepsilon_{2j}(x, y, z) = I_j(x, y, z)/I_{\text{in}}(x, y, z)$. The uniform distribution $U(1 - \xi_2, 1 + \xi_2)$, with the same mean and standard deviation of all nodes as n measurements related to $I_{\text{in}}(x, y, z)$, describes the disturbance of the actual field distribution of the pump source. The fluctuation range of the beam-pointing angle is the difference between the maximum and minimum measured values of the deviation angle of the far-field spot center in a single laser pulse width.

5. Design Method of Resonant Cavity Parameter with the Minimum Beam Pointing Drift Angle Fluctuation

In real-world applications, assessing the pumping parameters, such as the pumping power, pumping power disturbance factor, and pumping field disturbance factor poses minimum challenges. However, the resonator parameters, such as the radius of curvature R_1 for the output coupler, the radius of reflector mirror R_2, and the length of cavity L, requires further optimization according to the pumping parameters. In this study, we introduce a technique to compute optimum resonator parameters that result in the minimum beam-pointing drift-angle fluctuation range within a single pump duration.

We formulate the following technique:

- The calculation method is used to obtain the fluctuation range of the optical-axis offset angle with different R_1 and R_2 under the condition, that the pump source power and its disturbance are known – refer to Eq. (15), wherein R_1, R_2, the equation of motion of the light field, the output mode, and the optical-axis offset angle all change.

- This forms a two-dimensional data grid.

- The cubic spline interpolation method is used to obtain R_1 and R_2 with the minimum fluctuation range of the optical-axis offset angle.

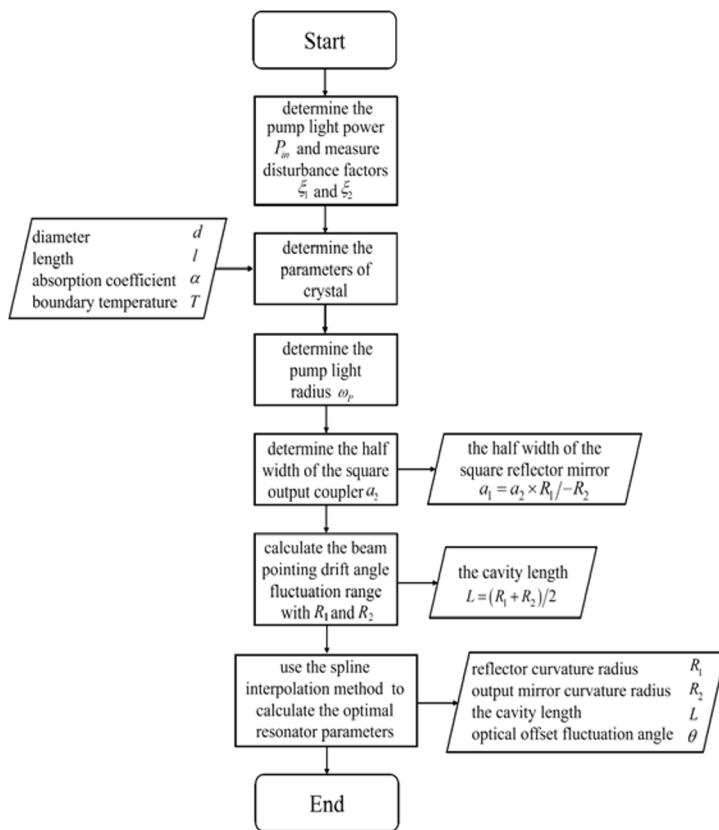The corresponding flowchart is presented in Fig. 13.

Fig. 13. Flow chart of the method for calculating the optimum resonator parameters.

First, measure the pumping power P_{in} and disturbance factors ξ_1 and ξ_2, and thus establish the physical parameters of the crystal. Next, determine the pump light radius ω_p and the half width of the square output coupler a_2. Derive half width of the square reflector mirror a_1, using the equation $a_1 = a_2 \times R_1/(-R_2)$ for the positive branch confocal unstable cavity. Next, calculate the beam pointing stability across a single pump duration, considering different values of R_1 and R_2, with the cavity length determined through the confocal equation $L = (R_1 + R_2)/2$ specific to the positive branch confocal unstable cavity. Finally, calculate the optimum resonator parameters employing the cubic spline interpolation method.

For instance, the computed outcomes of beam pointing drift angle fluctuation ranges with respect to R_1 and R_2 are displayed in Table 1, when $P_{\text{in}} = 10,000$ W, $\omega_p = 1.5$ mm, $a_1 = 0.6$ mm, $d = 10$ mm, $l = 10$ mm, $\alpha = 0.73$ mm^{-1}, and $\xi_1 = \xi_2 = 0.05$.

Table 1. Beam Pointing Drift Angle Fluctuation Range [in Radian] with R_1, R_2, and $L = (R_1 + R_2)/2$.

R_2	R_1					
	700 mm	800 mm	900 mm	1000 mm	1100 mm	1200 mm
-100 mm	$4.98 \cdot 10^{-4}$	$1.22 \cdot 10^{-4}$	$3.19 \cdot 10^{-4}$	$3.57 \cdot 10^{-4}$	$3.79 \cdot 10^{-4}$	$3.48 \cdot 10^{-4}$
-200 mm	$2.94 \cdot 10^{-4}$	$4.13 \cdot 10^{-4}$	$2.34 \cdot 10^{-4}$	$1.71 \cdot 10^{-4}$	$1.45 \cdot 10^{-4}$	$4.06 \cdot 10^{-4}$
-300 mm	$2.45 \cdot 10^{-4}$	$3.66 \cdot 10^{-4}$	$2.78 \cdot 10^{-4}$	$2.56 \cdot 10^{-4}$	$3.03 \cdot 10^{-4}$	$2.02 \cdot 10^{-4}$
-400 mm	$2.19 \cdot 10^{-4}$	$2.87 \cdot 10^{-4}$	$3.72 \cdot 10^{-4}$	$1.36 \cdot 10^{-4}$	$3.14 \cdot 10^{-4}$	$1.23 \cdot 10^{-4}$
-500 mm	$2.65 \cdot 10^{-4}$	$2.47 \cdot 10^{-4}$	$2.39 \cdot 10^{-4}$	$3.99 \cdot 10^{-4}$	$2.66 \cdot 10^{-4}$	$1.74 \cdot 10^{-4}$
-600 mm	$3.76 \cdot 10^{-4}$	$2.86 \cdot 10^{-4}$	$1.51 \cdot 10^{-4}$	$9.78 \cdot 10^{-4}$	$1.19 \cdot 10^{-4}$	$3.50 \cdot 10^{-4}$

Utilizing the cubic spline interpolation method, the optimum curvature radius of the reflector mirror R_1 and the output coupler R_2 are determined to be 1003 mm and -395 mm, respectively. This yields a corresponding optimum beam pointing drift angle fluctuation range of $1.18 \cdot 10^{-5}$ rad.

6. Conclusions

In this study, we proposed a numerical calculation model, which considered the instabilities and inhomogeneities within the thermal and gain distribution, to analyze the beam pointing instability in high-power solid-state lasers. We applied this model to assess the beam pointing instability of a quasi-continuously pumped Nd : YAG laser with positive branch confocal unstable resonator. The outcomes revealed that, when the pumping power resided within the range of $1000 - 25000$ W, and both the pumping power disturbance factor and pumping field disturbance factor have fallen within the range of $0.01 - 0.05$, the RMS value of the beam pointing drift angle varied within $1 \cdot 10^{-6} - 1 \cdot 10^{-4}$ rad. During a single pump duration, larger pumping field disturbance factors correlated with worsened beam pointing stability, whereas increased pumping power disturbance factors led to a broader range of variation in beam pointing stability. When $\xi_1 = 0.01$, $\xi_2 = 0.01 - 0.05$ and $P_{\text{in}} = 10,000$ W, the RMS value of the fluctuation range of beam pointing drift angle was $2 \cdot 10^{-5} - 1.2 \cdot 10^{-5}$ rad. Whereas, when $\xi_1 = 0.01 - 0.05$, $\xi_2 = 0.01$, and $P_{\text{in}} = 10,000 - 25,000$ W, the variation range of the RMS value of beam pointing stability was $8.83 \cdot 10^{-5} - 1.04 \cdot 10^{-5}$ rad.

The subsequent discussion addresses the optimization methodology for a resonant cavity operating with minimum beam pointing fluctuation. This approach considers instabilities and inhomogeneities of the thermal and gain distributions, exemplified through a numerical example featuring the calculation of the minimum beam pointing instability for a positive branch confocal unstable resonator with different curvature radii of reflector mirror R_1 and output coupler R_2. The results indicated that, under certain conditions, specifically $\xi_1 = \xi_2 = 0.05$ and $P_{\text{in}} = 10,000$ W, the optimum curvature radius $R_1 = 1003$ mm and $R_2 = -395$ mm, thus resulting in the achievement of a minimum beam pointing drift angle fluctuation of $1.18 \cdot 10^{-5}$ rad.

This study provides a rational and efficient framework for evaluating beam pointing instability in high-power solid-state lasers, along with designing resonant cavity parameters to minimize beam pointing fluctuation. The approach boasts have the benefits of straightforward design and wide-ranging applicability. Theoretically, it can be extended to solid-state lasers utilizing resonators and laser crystals beyond the positive branch confocal unstable resonator and Nd : YAG crystal.

Acknowledgments

References

1. W. Liu, Y. Niu, H. Liu, et al., *Opt. Eng.*, **53**, 026102 (2014).
2. M. Bass and J. Dong, *IEEE J. Quantum Electron.*, **41**, 183 (2005).
3. G. Boulon, *Opt. Mater.*, **34**, 499 (2011).
4. G. Huber, C. Kränkel, and K. Petermann, *J. Opt. Soc. Am. B*, **27**, B93 (2010).
5. X. Tang, G. Wang, J. Liu, et al., *Strateg. Study Chin. Acad. Eng.*, **22**, 49 (2020); DOI: 10.15302/J-SSCAE-2020.03.008
6. D. Dhupal, B. Doloi, and B. Bhattacharyya, *Opt. Lasers Eng.*, **47**, 917 (2009).
7. P. Mahnke, P. Peuser, and P. Huke, *Appl. Phys.*, **B116**, 333 (2014).
8. C. Chagnot, G. D. Dinechin, and G. Canneau, *Nucl. Eng. Des.*, **240**, 2604 (2010).
9. H. Xiang, B. Chen, W. Wu, et al., *Int. J. Heat Mass Transf.*, **114**, 1220 (2017).
10. T. Andreas, B. Marcus, and K. Gerhard, *Opt. Eng.*, **56**, 124104 (2017).
11. C. Posadas-Castillo, R. M. López-Gutiérrez, and C. Cruz-Hernández, *Commun. Nonlinear Sci. Numer. Simul.*, **13**, 1655 (2007).
12. J. Xu, M. Kong, A. Lin, et al., *Opt. Lett*, **42**, 1664 (2017).
13. L. Ding, S. Li, Z. Lu, et al., *Optik*, **127**, 6056 (2016).
14. M. Xie, P. Liu, C. Ma, et al., *Optik*, **183**, 775 (2019).
15. S. K. Dixit, R. Mahakud, O. Prakash, et al., *Opt. Commun.*, **281**, 2590 (2018).
16. S. J. DeSilva and C. L. Chan, *Appl. Mat. Model.*, **32**, 2429 (2008).
17. Y. Gu, Q. Hua, C. Zhang, and X. He, *Appl. Math. Model.*, **71**, 316 (2019).
18. D. S. de Oliveira and F. B. Ribeiro, *J. Heat Transf.*, **133**, 062301 (2011).
19. J. W. Goodman, *Introduction to Fourier Optics*, 2nd edition, The McGraw-Hill Companies Inc., New York (1996), p. 461.
20. M. Born and E. Worf, *Principles of Optics*, 7th edition, Cambridge University Press, Oxford (1999), p. 412516; 633673.
21. A. H. Paxton and C. Yang, *LASER*, **10090**, 233 (2017).
22. A. A. Ishaaya, N. Davidson, G. Machavariani, et al., *IEEE J. Quantum Electron.*, **39**, 74 (2003).
23. A. P. Ongstad, R. Kaspi, G. C. Dente, et al., *Appl. Phys. Lett.*, **90**, 191107 (2007).

24. X. Zhang, J. Wang, and Z. Hu, *Optik*, **127**, 3912 (2016).

25. X. Zhang, *Adv. Mater. Res.*, vol. 301–303, Trans Tech Publications, Ltd., July 2011, pp. 1351–1355.

26. C. Pfistner and R. Weber, *IEEE J. Quantum Electron.*, **30**, 1605 (1994).

27. S. Li, Y. Li, S. Zhao, et al., *Opt. Laser Technol.*, **68**, 146 (2015).

28. E. Zieniuk and D. Sawick, *J. Heat Transf.*, **139**, 081301 (2017).